AIAA JOURNAL
Vol. 34, No. 10, October 1996

Higher-Order Numerical Model for Simulation of Time-Dependent Variable-Density Flows

Jyh-Cherng Sheu* and Lea-Der Chen†
University of Iowa, Iowa City, Iowa 52242-1527

A numerical model, first-order accurate in time discretization and second-order accurate in space discretization, is presented for the simulation of time-dependent laminar diffusion flames. The numerical model uses a semi-implicit scheme for time marching and incorporates flux-corrected transport (FCT) for convection terms and projection method for velocity-pressure coupling. A direct solver is used for solving the pressure Poisson equation. A time-splitting method is adopted to split the transport equation into a convection equation in explicit form and a diffusion equation in implicit form. The explicit convection equation allows for implementation of the FCT without introducing an artificial viscosity. The implicit diffusion equation removes the time step size restriction of the von Neumann stability criterion. Theoretical assessments are derived for the order of accuracy of time difference by viewing the projection method as a lower-upper decomposition, and formulation is also given to establish the second-order accuracy. The current numerical model is used to solve the Smith–Hutton problem and the Burke–Schumann diffusion flame with or without external forcing of the fuel jet. The results are compared with solutions using the schemes of lower-order accuracy in the space discretization. The comparison shows that significant numerical diffusion error exists in the solution when a first-order upwind difference scheme or power-law approximation is used. The present study suggests that a higher-order space difference scheme should be used for the simulation of time-dependent laminar jet diffusion flames, although a first-order time difference scheme would be adequate.

Nomenclature

b	= coupling function; Eq. (7)
Cp	= specific heat
D	= binary diffusion coefficient
D_i	= diffusion number; Eq. (25)
F/O	= fuel oxidant ratio; Eq. (7)
g	= acceleration of the gravity
H	= total enthalpy; Eq. (8)
h	= thermal enthalpy
J	= convection operator; Eq. (10)
L	= diffusion operator; Eq. (10)
Le	= Lewis number
N	= number of species
Pe	= Peclet number
p	= pressure
Re	= Reynolds number
Ri	= Richardson number
r	= radial coordinate
S	= source term
t	= time
u	= axial velocity
v	= radial velocity
x	= axial coordinate
Γ	= diffusivity; Eq. (2)
$\Delta h^0_{f,i}$	= enthalpy of formulation of ith species
κ	= thermal conductivity
μ	= dynamic viscosity
ρ	= density
ϕ	= scalar
ψ	= generic variable; Eq. (21)

Subscripts

F_∞	= initial fuel stream
i	= species i
m	= mixture
O_∞	= initial oxidant stream
0	= reference state

Superscripts

n	= time step
$*$	= intermediate value; Eq. (15)
$**$	= intermediate value; Eq. (21)

Received July 8, 1995; revision received May 28, 1996; accepted for publication June 9, 1996.

*Research Associate, Department of Mechanical Engineering.
†Professor and Chair, Department of Mechanical Engineering. Member AIAA.

Introduction

THE accuracy of a numerical model is central to the interpretation of the results. To improve the accuracy associated with truncation error in the discretization of the governing equation, smaller time-step and/or finer grid resolutions can be used. The computational time, however, increases as a result of the refinements of temporal and grid resolution. An alternate to finer discretization is to adopt a higher-order accurate numerical scheme. The higher-order accurate schemes (e.g., order higher than 1), however, are also known for the tendency to produce nonphysical dispersions or oscillations in the solution. The numerical diffusion and oscillation errors can artificially suppress or amplify the instabilities in an unsteady or time-dependent flow; thus, it may overwhelm the physics of the fluid flow or the heat transfer being studied. Therefore, the robustness of a numerical model is of particular importance to the simulation of time-dependent flow. In this paper, a higher-order accurate numerical model with an oscillation-free solution is presented. The robustness of the current numerical model is demonstrated in the simulation of a time-dependent axisymmetric laminar jet diffusion flame. The diffusion flame example is chosen because of the sharp variations in such properties as density, specific heat, viscosity, and thermal conductivity near the stoichiometric (or flame) surface, which present a stringent test case for the numerical model.

There exist several investigations on the dynamic characteristics of laminar jet diffusion flames based on numerical investigations. For example, an explicit time difference scheme, along with quadratic upwind approximations for the convection term, was used in the study of the dynamic structure of a buoyant jet diffusion flame.[1–4] The order of accuracy of the numerical model in Refs. 1–4 is temporally first order and spatially second order. The second-order approximation adopted the QUICK scheme[5] and the central difference for the convection and diffusion terms, respectively. Although

the simulation results of Refs. 2–4 are verified by experimental data, the QUICK scheme does not guarantee monotonic and stable solutions, as has been shown by Sharif and Busnaina[6] and Sharif.[7] The QUICK scheme has a tendency to produce overshoots and undershoots in the solution (or nonphysical dispersions); the solution therefore may be contaminated. The computational effort is also expensive. To improve the computational efficiency, Wu and Chen[8] used power-law approximations to replace the QUICK scheme in the numerical model of Ref. 2. This modified numerical model[8] was able to reproduce the dynamic characteristics of the near-laminar, nitrogen-diluted propane jet diffusion flame,[2–4] as well as the flicker frequency of an experimental, time-dependent wick diffusion flame.[8] The order of accuracy of the numerical model of Ref. 8 was temporally first order and spatially "nearly second order" because the power-law scheme combines the first-order upwind and second-order central difference in the discretization. The power-law approximation does not guarantee second-order accuracy of the solution because it becomes a first-order upwind scheme when the grid Peclet number exceeds 10; thus, the power-law scheme is known for possible numerical diffusion error in the solution; e.g., see Ref. 9.

To study the effects of gravitational force and nonunity Lewis number on laminar jet diffusion flames, Katta et al.[10,11] used the implicit time marching and the hybrid and QUICKEST schemes in the numerical model. The hybrid scheme was taken from Spalding[12] and was used to treat the convective transport of scalars (i.e., species and energy). The QUICKEST scheme[5] was used for the convective transport of momentum. The implicit time marching removed the time-step limitation of Courant–Friedrichs–Lewy (CFL) condition and improved the computational efficiency. However, linearization of the convection term in the implicit scheme has implications on the order of accuracy of the solution. The order of accuracy of a hybrid scheme is not unconditionally second order; the scheme becomes first-order upwind when the grid Peclet number exceeds 2. The QUICKEST scheme is spatially second-order accurate; however, it does not guarantee monotonic and stable solutions. The order of accuracy of the numerical model of Refs. 10 and 11 is therefore temporally first order and spatially nearly second-order. To remove the nonphysical oscillations produced by higher-order schemes, the flux-corrected transport (FCT) developed by Boris[13] and Boris and Book[14] has been successfully incorporated in the simulation of jet diffusion flames.

The FCT algorithm is an explicit finite difference scheme. The numerical time step is limited by the speed of sound based on the CFL condition. This restriction makes the computation of a slowly time-evolving flow extremely expensive.[15] To remedy this deficiency, Patnaik et al.[16] developed a "barely implicit correction" algorithm for the flux-corrected transport known as the BIC-FCT. The BIC-FCT takes a novel approach on time difference. In short, only the terms containing pressure in the momentum equations and velocity in the energy equation are treated by implicit scheme. Therefore, the numerical time step restricted by the CFL condition is based on the fluid velocity, not the speed of sound. As a result, the time step is shown to increase by 50 times.[16] The order of accuracy of BIC-FCT is first order in time differencing, and higher order in space differencing can be obtained without nonphysical oscillations or dispersions in the solution. The BIC-FCT is successfully used by Ellzey et al.[15] and Kaplan et al.[17] for simulation of the time-dependent jet diffusion flame. The diffusion term is treated explicitly, and the restriction of the von Neumann stability condition resulting from the explicit treatment is relaxed by subcycling the diffusion subroutine.[15,17]

For an explicit time-marching scheme without subcycling for the diffusion term, the time-step restriction as a result of the von Neumann instability criterion may be more rigorous than that imposed by the CFL condition, depending on the Reynolds number and geometry of the flow. Generally, a more stringent von Neumann stability condition is required for internal flow calculations. The time-step restriction as a result of von Neumann or CFL constraints can be relaxed if a fully implicit time difference scheme is used. The fully implicit scheme, however, has its own drawbacks. For example, the computational effort could be overwhelming because of the iterative predictor-corrector procedure in the updating of nonlinear convection terms. Therefore, a semi-implicit scheme is appealing for the simulation of diffusion-dominated flows (or convection-diffusion flows to a lesser degree) because it does not require the use of an iterative procedure to update the convective flux; the von Neumann constraint is relaxed.

In this paper, we present a semi-implicit numerical scheme for simulation of the time-dependent variable-density flows. A low-speed laminar jet diffusion flame is used as an example. The numerical code adopts an explicit scheme for the convection term and an implicit scheme for the diffusion term. Thus, the code allows for the implementation of FCT independent of the difference schemes used for the diffusion term. Both first- and second-order schemes for space discretization are used to illustrate that numerical diffusion error as a result of a first-order upwind scheme can severely contaminate the solution. The temporal accuracy is evaluated from theoretical considerations. Because the projection method is used for the velocity and pressure coupling, additional assessment of the order of accuracy is necessary in solving the pressure Poisson equation. Namely, when one views the projection method as a lower-upper (LU) decomposition, the order of accuracy can accordingly be assessed. The objectives of this paper are 1) to present a numerical model for the simulation of low-speed, time-dependent, and variable-property flows, 2) to estimate the order of accuracy when the projection method is used and variable properties are fully accounted for, and 3) to illustrate the effects of the order of accuracy on the simulation. A wall-bounded jet diffusion flame of the classical Burke–Schumann diffusion flame (BSDF)[18] is used as an example of the variable-property flow, and a low-frequency periodic perturbation (e.g., 1 or 2 Hz) is imposed on the fuel-jet exit velocity to introduce unsteadiness in the flow.

Mathematical Formulation

The mathematical formulation is based on the time-dependent axisymmetric variable-density flow, and variable properties are fully accounted for. The major assumptions are negligible radiative heat transfer and viscous dissipation, low Mach number, and laminar Newtonian flow. Based on these assumptions, the numerical model solves the transport equations for the conservation of mass, scalar (i.e., energy or species), and momentum. The dimensionless equations are summarized next.

Continuity:

$$\frac{\partial(r\rho)}{\partial t}+\frac{\partial(r\rho u)}{\partial x}+\frac{\partial(r\rho v)}{\partial r}=0 \tag{1}$$

Scalar:

$$\frac{\partial(r\rho\phi)}{\partial t}+\frac{\partial(r\rho u\phi)}{\partial x}+\frac{\partial(r\rho v\phi)}{\partial r}=\frac{\partial}{\partial x}\left(r\Gamma_{\phi x}\frac{\partial\phi}{\partial x}\right)+\frac{\partial}{\partial r}\left(r\Gamma_{\phi r}\frac{\partial\phi}{\partial r}\right)+S_\phi \tag{2}$$

Momentum:

$$\frac{\partial(r\rho u)}{\partial t}+\frac{\partial(r\rho uu)}{\partial x}+\frac{\partial(r\rho vu)}{\partial r}=-r\frac{\partial p}{\partial x}+\frac{1}{Re}\left[\frac{\partial}{\partial x}\left(r\frac{4\mu}{3}\frac{\partial u}{\partial x}\right)+\frac{\partial}{\partial r}\left(r\mu\frac{\partial u}{\partial r}\right)\right]+S_u \tag{3}$$

$$\frac{\partial(r\rho v)}{\partial t}+\frac{\partial(r\rho uv)}{\partial x}+\frac{\partial(r\rho vv)}{\partial r}=-r\frac{\partial p}{\partial r}+\frac{1}{Re}\left[\frac{\partial}{\partial x}\left(r\mu\frac{\partial v}{\partial x}\right)+\frac{\partial}{\partial r}\left(r\frac{4\mu}{3}\frac{\partial v}{\partial r}\right)\right]+S_v \tag{4}$$

The model parameters Γ and S are

$$\Gamma_{\phi x}=\Gamma_{\phi r}=(1/Pe)(\kappa/Cp) \quad \text{when} \quad \phi=h$$

$$\Gamma_{\phi x}=\Gamma_{\phi r}=(1/PeLe)\rho D \quad \text{when} \quad \phi=Y_i$$

$$S_\phi=-\frac{L_0}{\rho_0U_0}\sum_{i=1}^{N}r\dot{\omega}_i\frac{\Delta h_{f,i}^0}{h_0} \quad \text{when} \quad \phi=h$$

$$S_\phi=(L_0/\rho_0U_0)r\dot{\omega}_i \quad \text{when} \quad \phi=Y_i$$

$$S_u = \frac{1}{Re}\left[\frac{\partial}{\partial r}\left(r\mu\frac{\partial v}{\partial x}\right) - \frac{2}{3}\frac{\partial}{\partial x}\left(\mu\frac{\partial(rv)}{\partial r}\right)\right] - r\rho Ri$$

$$S_v = \frac{1}{Re}\left\{\frac{\partial}{\partial x}\left(r\mu\frac{\partial u}{\partial r}\right) - \frac{2}{3}\left[\frac{\partial}{\partial r}\left(r\mu\frac{\partial u}{\partial x}\right) + v\frac{\partial\mu}{\partial r} + \mu\left(\frac{2v}{r} - \frac{\partial u}{\partial x}\right)\right]\right\}$$

In the preceding equations, u and v are the velocity components in the x and r directions, respectively, $\dot{\omega}_i$ is the mass reaction rate of species i, and Y_i is the mass fraction of species i. The transport equations are normalized by characteristic length L_0, velocity U_0, pressure $\rho_0 U_0^2$, and enthalpy h_0, along with reference properties of ρ_0, μ_0, Cp_0, and D_0. The resulting dimensionless parameters are the Reynolds number, Peclet number, Lewis number, and Richardson number, respectively, defined as

$$Re = \frac{\rho_0 U_0 L_0}{\mu_0}, \qquad Pe = \frac{U_0 L_0 \rho_0 Cp_0}{\kappa_0}$$

$$Le = \frac{\kappa_0}{\rho_0 Cp_0 D_0}, \qquad Ri = \frac{L_0 g}{U_0^2}$$

A flame-sheet model is used to calculate the thermochemical properties of the flame, and the ideal gas assumption is invoked. The flame-sheet model assumes an infinitely large Damkohler number (i.e., fast chemistry), equal diffusion coefficients for all species, and a unity Lewis number for the mixture. It is further assumed that the flame is adiabatic, and a one-step irreversible chemical reaction occurs in an infinitely thin region with CO_2 and H_2O being the only combustion products. With these assumptions, the Shvab–Zeldovich formulation[19] can be used; namely, a single conserved scalar, or the mixture fraction, is used to combine the energy and species equations. The mixture fraction is defined as

$$f = \frac{[b]_m - [b]_{O_\infty}}{[b]_{F_\infty} - [b]_{O_\infty}} \tag{5}$$

or

$$f = \frac{[H]_m - [H]_{O_\infty}}{[H]_{F_\infty} - [H]_{O_\infty}} \tag{6}$$

where subscripts st, m, O_∞, and F_∞ denote the stoichiometric condition, the local mixture condition, the oxidant stream at $x = 0$ and $r = \infty$, and the fuel stream at $x = 0$, respectively. Parameters b and H are defined as

$$b = Y_F - (F/O)_{st} Y_O \tag{7}$$

$$H = h + \sum_{i=1}^{N} Y_i \Delta h_{f,i}^0 \tag{8}$$

When Eq. (2) is used to solve the transport equation of the mixture fraction, the corresponding model parameters are

$$\Gamma_{fx} = \Gamma_{fr} = (1/Pe)(\kappa/Cp) \qquad S_f = 0$$

To account for the temperature-dependent property variation (i.e., density, specific heat, viscosity, and thermal conductivity), we adopted the property correlations used in Ref. 20 for the calculation.

Numerical Method

The current numerical method employs a finite volume formulation, staggered grids, and semi-implicit time marching. A projection method is used for the velocity and pressure coupling, and the resultant pressure Poisson equation is solved by a direct solver. To reduce (or eliminate) spurious oscillations in the solution, FCT is applied to the convective flux. Based on staggered grids, the velocities are defined at the surface of the finite volume, and the scalar quantities (i.e., mixture fraction, pressure, thermodynamics, and transport properties) are defined at the center of the finite volume. The advantage of using staggered grids is that the pressure boundary condition is not required.[21,22] The pressure boundary condition can be replaced by specifying the velocity components normal to the boundary. The semi-implicit scheme treats the convection and source terms explicitly and the diffusion term implicitly. Depending on the explicit or implicit schemes used in the discretization of convection and diffusion terms, a higher-order accurate numerical model can be derived as discussed in the following.

Using the solution at the previous time step for the convection and source terms, and that at the current time step for the diffusion term, the discretized transport equations, i.e., Eqs. (1–4), assume the following form.

Continuity:

$$\frac{(r\rho)^{n+1} - (r\rho)^n}{\Delta t} + \frac{\partial(r\rho u)^{n+1}}{\partial x} + \frac{\partial(r\rho v)^{n+1}}{\partial r} = 0 \tag{9}$$

Scalar:

$$\frac{(r\rho\phi)^{n+1} - (r\rho\phi)^n}{\Delta t} + J(r\rho^n\phi^n) = L_\phi(r\rho^{n+1}\phi^{n+1}) \tag{10}$$

Momentum:

$$\frac{(r\rho u)^{n+1} - (r\rho u)^n}{\Delta t} + J(r\rho^n u^n) = -r\left(\frac{\partial p}{\partial x}\right)^{n+1} + L_u(r\rho^{n+1}u^{n+1}) + S_u^n \tag{11}$$

$$\frac{(r\rho v)^{n+1} - (r\rho v)^n}{\Delta t} + J(r\rho^n v^n) = -r\left(\frac{\partial p}{\partial r}\right)^{n+1} + L_v(r\rho^{n+1}v^{n+1}) + S_v^n \tag{12}$$

where

$$J = \frac{\partial}{\partial x}u + \frac{\partial}{\partial r}v$$

$$L_\phi = \frac{\partial}{\partial x}\left(\frac{r}{Pe}\frac{\kappa}{Cp}\frac{\partial}{\partial x}\frac{1}{r\rho}\right) + \frac{\partial}{\partial r}\left(\frac{r}{Pe}\frac{\kappa}{Cp}\frac{\partial}{\partial r}\frac{1}{r\rho}\right)$$

$$L_u = \frac{\partial}{\partial x}\left(\frac{r}{Re}\frac{4\mu}{3}\frac{\partial}{\partial x}\frac{1}{r\rho}\right) + \frac{\partial}{\partial r}\left(\frac{r}{Re}\mu\frac{\partial}{\partial r}\frac{1}{r\rho}\right)$$

and

$$L_v = \frac{\partial}{\partial x}\left(\frac{r}{Re}\mu\frac{\partial}{\partial x}\frac{1}{r\rho}\right) + \frac{\partial}{\partial r}\left(\frac{r}{Re}\frac{4\mu}{3}\frac{\partial}{\partial r}\frac{1}{r\rho}\right)$$

In the preceding equations, subscripts n and $n+1$ denote variables evaluated at the previous and current time steps. The scalar quantity ϕ in Eq. (10) represents the mixture fraction in the current numerical model, whereas energy or species concentration can be used for ϕ when finite rate chemistry is considered.

The pressure gradient terms in Eqs. (11) and (12) remain unknown and need special treatment. The velocity and pressure coupling is solved based on the projection method (or the fractional step method). Following Perot,[23] the projection method is viewed as an LU decomposition instead of the time splitting of Kim and Moin.[24] For example, Eqs. (9), (11), and (12), along with respective boundary conditions, can be cast into the following matrix form:

$$\begin{bmatrix} A_u & 0 & r\dfrac{\partial}{\partial x} \\ 0 & A_v & r\dfrac{\partial}{\partial r} \\ \dfrac{\partial}{\partial x} & \dfrac{\partial}{\partial r} & 0 \end{bmatrix} \begin{bmatrix} (r\rho u)^{n+1} \\ (r\rho v)^{n+1} \\ p^{n+1} \end{bmatrix} = \begin{bmatrix} S_u^n - J(r\rho^n u^n) \\ S_v^n - J(r\rho^n v^n) \\ -r/\Delta t(\rho^{n+1} - \rho^n) \end{bmatrix} + \begin{bmatrix} BC_u \\ BC_v \\ BC_p \end{bmatrix} \tag{13}$$

where

$$A_u = (1/\Delta t)(1 - \Delta t L_u) \tag{13a}$$

and

$$A_v = (1/\Delta t)(1 - \Delta t L_v) \tag{13b}$$

The right-hand side of Eq. (13) contains all of the quantities that are already known. The first matrix in the left-hand side of Eq. (13) can be approximated as a multiplication of two submatrices, yielding

$$\begin{Bmatrix} A_u & 0 & 0 \\ 0 & A_v & 0 \\ \dfrac{\partial}{\partial x} & \dfrac{\partial}{\partial r} & -\left[\dfrac{\partial}{\partial x}\left(B_u r \dfrac{\partial}{\partial x}\right)+\dfrac{\partial}{\partial r}\left(B_v r \dfrac{\partial}{\partial r}\right)\right] \end{Bmatrix} \times \begin{bmatrix} 1 & 0 & B_u r \dfrac{\partial}{\partial x} \\ 0 & 1 & B_v r \dfrac{\partial}{\partial r} \\ 0 & 0 & 1 \end{bmatrix} \begin{bmatrix} (r\rho u)^{n+1} \\ (r\rho v)^{n+1} \\ p^{n+1} \end{bmatrix} = \begin{bmatrix} S_u^n - J(r\rho^n u^n) \\ S_v^n - J(r\rho^n v^n) \\ -r/\Delta t(\rho^{n+1}-\rho^n) \end{bmatrix} + \begin{bmatrix} BC_u \\ BC_v \\ BC_p \end{bmatrix} \tag{14}$$

The truncation errors are, respectively,

$$(A_u B_u - 1) r \frac{\partial}{\partial x} p^{n+1} \qquad \text{and} \qquad (A_v B_v - 1) r \frac{\partial}{\partial r} p^{n+1}$$

for axial and radial components of the momentum equation. The order of the truncation error can be determined by properly assigning values to B_u and B_v. For example, when one sets B_u and B_v to Δt, the truncation errors are, respectively,

$$-\Delta t L_u\left(r \frac{\partial}{\partial x} p^{n+1}\right) \qquad \text{and} \qquad -\Delta t L_v\left(r \frac{\partial}{\partial r} p^{n+1}\right)$$

The discretized approximation is therefore first-order accurate in time discretization.

Using LU decomposition, Eq. (14) is factored into

$$\begin{Bmatrix} A_u & 0 & 0 \\ 0 & A_v & 0 \\ \dfrac{\partial}{\partial x} & \dfrac{\partial}{\partial r} & -\left[\dfrac{\partial}{\partial x}\left(B_u r \dfrac{\partial}{\partial x}\right)+\dfrac{\partial}{\partial r}\left(B_v r \dfrac{\partial}{\partial r}\right)\right] \end{Bmatrix} \begin{bmatrix} (r\rho)^{n+1}u^* \\ (r\rho)^{n+1}v^* \\ p^{n+1} \end{bmatrix} = \begin{bmatrix} S_u^n - J(r\rho^n u^n) \\ S_v^n - J(r\rho^n v^n) \\ -r/\Delta t(\rho^{n+1}-\rho^n) \end{bmatrix} + \begin{bmatrix} BC_u \\ BC_v \\ BC_p \end{bmatrix} \tag{15a}$$

and

$$\begin{bmatrix} 1 & 0 & B_u r \dfrac{\partial}{\partial x} \\ 0 & 1 & B_v r \dfrac{\partial}{\partial r} \\ 0 & 0 & 1 \end{bmatrix} \begin{bmatrix} (r\rho u)^{n+1} \\ (r\rho v)^{n+1} \\ p^{n+1} \end{bmatrix} = \begin{bmatrix} (r\rho)^{n+1}u^* \\ (r\rho)^{n+1}v^* \\ p^{n+1} \end{bmatrix} \tag{15b}$$

The intermediate velocities u^* and v^* are solved from Eq. (15a). The boundary conditions are already implemented before LU decomposition takes place [cf. Eq. (13)]; therefore, the LU factorization does not need additional boundary conditions during the solution for intermediate variables or pressure.

Substituting A_u and A_v from Eqs. (13a) and (13b) into Eqs. (15a) and (15b), one obtains the following set of equations:

$$\frac{(r\rho)^{n+1}u^* - (r\rho u)^n}{\Delta t} + J(r\rho^n u^n) = L_u(r\rho^{n+1}u^*) + S_u^n \tag{16}$$

$$\frac{(r\rho u)^{n+1} - (r\rho)^{n+1}u^*}{\Delta t} = -r\frac{\partial p^{n+1}}{\partial x} \tag{17}$$

$$\frac{(r\rho)^{n+1}v^* - (r\rho v)^n}{\Delta t} + J(r\rho^n v^n) = L_v(r\rho^{n+1}v^*) + S_v^n \tag{18}$$

$$\frac{(r\rho v)^{n+1} - (r\rho)^{n+1}v^*}{\Delta t} = -r\frac{\partial p^{n+1}}{\partial r} \tag{19}$$

as well as the pressure Poisson equation

$$\nabla^2 p^{n+1} = \frac{(\rho^{n+1}-\rho^n)}{\Delta t^2} + \frac{1}{\Delta t}\left[\frac{\partial}{\partial x}(r\rho^{n+1}u^*) + \frac{1}{r}\frac{\partial}{\partial r}(r\rho^{n+1}v^*)\right] \tag{20}$$

The spatial accuracy of the current numerical model depends on the specific schemes used to discretize the spatial derivatives in Eqs. (10), (16), and (18). If a lower-order scheme is used, a finer grid resolution is necessary to reduce the numerical diffusion error. When a higher-order scheme is used, special efforts are warranted to reduce or prevent nonphysical dispersions or oscillations in the solution. The current semi-implicit numerical model adopts the FCT correction for the convective flux. The FCT scheme was initially developed for explicit schemes. The coupling to a fully implicit scheme is reported in a recent study of the vortex and diffusion flame interaction by Laverdant and Candel.[25] It was also cautioned[25] that the simultaneous use of an alternating direction implicit (ADI) scheme and a diffusion-antidiffusion filter may introduce an artificial viscosity; therefore, the model accuracy may be contaminated. The time-splitting method is used in the current numerical model to remove the artificial viscosity.

Using the time splitting, the transport equations, i.e., Eqs. (10), (16), and (18), are split into two subequations. The convection equation is cast into an explicit form and the diffusion equation into an implicit form:

$$\frac{(r\rho)^{n+1}\psi^{**} - (r\rho\psi)^n}{\Delta t} + J(r\rho^n\psi^n) = S_\psi^n \tag{21}$$

$$\frac{(r\rho)^{n+1}\psi^* - (r\rho)^{n+1}\psi^{**}}{\Delta t} = L_\psi(r\rho^{n+1}\psi^*) \tag{22}$$

where ψ denotes ϕ, u, or v, and when $\psi = \phi$, superscript $*$ is set to $n+1$. In the current numerical code, we adopted the FCT developed by Zalesak[26] for the convective flux in Eq. (21), along with QUICK scheme to be our higher-order (i.e., second-order) discretization. The current numerical model is coded such that the QUICK scheme can be substituted by first-order upwind or higher-order schemes, independent of the treatment of the diffusion term. The diffusion term in Eq. (22) is discretized using a second-order central difference, which has a stabilizing effect on the solution. The ψ^{**} value obtained using the FCT is treated as the source term in Eq. (22), which is solved by the ADI method.

Temporal Order of Accuracy

Higher-order temporal accuracy can be achieved using the current numerical scheme. For example, the first-order time discretization of the continuity equation can be replaced by a second-order implicit Crank–Nicolson,[27] and the first-order time discretization of scalar transport (e.g., transport of mixture fraction, energy, or species concentration) can be replaced by a second-order explicit leapfrog-trapezoidal scheme[28] for the convection term and a second-order implicit Crank–Nicolson[27] for the diffusion term. Similarly, the momentum equation solver can be made second-order accurate by adopting a second-order explicit Adam–Bashforth scheme[22] for the convection term and a second-order implicit Crank-Nicolson[27] for the diffusion term. Equation (13) then becomes

$$\begin{bmatrix} A_u & 0 & r\dfrac{\partial}{\partial x} \\ 0 & A_v & r\dfrac{\partial}{\partial r} \\ \dfrac{\partial}{\partial x} & \dfrac{\partial}{\partial r} & 0 \end{bmatrix} \begin{bmatrix} (r\rho u)^{n+1} \\ (r\rho v)^{n+1} \\ p^{n+1} \end{bmatrix} = \begin{Bmatrix} S_u^n - \frac{3}{2}J(r\rho^n u^n) + \frac{1}{2}J(r\rho^{n-1}u^{n-1}) + \frac{1}{2}L_u(r\rho^n u^n) \\ S_v^n - \frac{3}{2}J(r\rho^n v^n) + \frac{1}{2}J(r\rho^{n-1}v^{n-1}) + \frac{1}{2}L_v(r\rho^n v^n) \\ -\dfrac{2r}{\Delta t}(\rho^{n+1}-\rho^n) - \left[\dfrac{\partial}{\partial x}(r\rho^n u^n) + \dfrac{\partial}{\partial r}(r\rho^n v^n)\right] \end{Bmatrix} + \begin{bmatrix} BC_u \\ BC_v \\ BC_p \end{bmatrix} \tag{23}$$

where

$$A_u = (1/\Delta t)[1 - (\Delta t/2)L_u] \tag{23a}$$

and

$$A_v = (1/\Delta t)[1 - (\Delta t/2)L_v] \tag{23b}$$

The coefficient matrix of Eq. (23) has the same form as that of Eq. (13); therefore, the truncation error remains the same. Conversely, the truncation error is $(A_u B_u - 1)r(\partial/\partial x)p^{n+1}$ and $(A_v B_v - 1)r(\partial/\partial r)p^{n+1}$ for the axial and radial components of the momentum equation, respectively. A proper choice of B_u and B_v is necessary to maintain the temporal second-order accuracy because of the usage of the projection method for the pressure and velocity coupling. Without properly prescribed B_u and B_v, the overall order of accuracy will deteriorate regardless of the order of accuracy of the time difference scheme that is used. To obtain the second-order temporal accuracy, B_u and B_v are specified to be

$$B_u = \Delta t[1 + (\Delta t/2)L_u]$$

and

$$B_v = \Delta t[1 + (\Delta t/2)L_v] \tag{24}$$

The resultant truncation errors as a result of factorization are, respectively,

$$-\frac{\Delta t^2}{4}L_u^2\left(r\frac{\partial}{\partial x}p^{n+1}\right) \quad \text{and} \quad -\frac{\Delta t^2}{4}L_v^2\left(r\frac{\partial}{\partial r}p^{n+1}\right)$$

consequently, the second-order accuracy is achieved in the time difference.

When the numerical model is made temporally second-order accuracy, the computational efficiency is greatly compromised because of the direct solver used for the pressure Poisson equation. The current numerical model requires that the coefficient matrix of the direct solver [cf. Eq. (20)] be calculated only once. When the second-order accuracy is considered for time discretization, the coefficient matrix needs to be updated for each time step; the time-varying viscosity that appears in L_u and L_v needs to be updated when B_u and B_v are substituted into Eq. (15). The CPU time required for calculation of the coefficient matrix is too demanding for the current numerical model (also see discussions in Refs. 1–4, 8, 10, and 11). Thus, second-order accuracy in time difference is not used. The use of the first-order accurate schemes for time difference is justified based on prior validations of the first-order schemes for the simulation of time-varying, laminar jet diffusion flames.[1–4,8,10,11] When an infinitely fast chemistry assumption is invoked, the simulation usually requires a time step of 0.1 ms. This time step size is sufficient to capture the dynamics of a laminar flame. A much smaller time step is needed when finite rate chemical reactions are considered. Thus, the current numerical model adopts a first-order scheme for time difference, although a higher-order scheme is presented. The solution procedure of the current numerical model first solves ϕ at the beginning of each iterative time step. Intermediate velocities u^* and v^* are calculated from Eqs. (16) and (18) and substituted into the right-hand side of Eq. (20) for calculating the velocity-pressure coupling or solving the pressure Poisson equation. Finally, the velocities at the current time step are updated by Eqs. (17) and (19).

Model Verification and Assessment

Smith–Hutton Problem

The numerical model is used to solve the Smith–Hutton problem[29] to test the coupling of the semi-implicit scheme with FCT and to assess the numerical diffusion error. The Smith–Hutton test case (Fig. 1), which has been used for comparative evaluation of numerical schemes by Smith and Hutton[29] and Sharif,[7] yields solutions with flow recirculation and sharp changes of convected variables over a short distance. Thus, it is meaningful to use the Smith–Hutton problem to assess the numerical diffusion error. The Smith–Hutton test case solves the following (dimensionless) elliptic equation:

$$u\frac{\partial\phi}{\partial x} + v\frac{\partial\phi}{\partial y} = \frac{1}{D_i}\left(\frac{\partial^2\phi}{\partial x^2} + \frac{\partial^2\phi}{\partial y^2}\right) \tag{25}$$

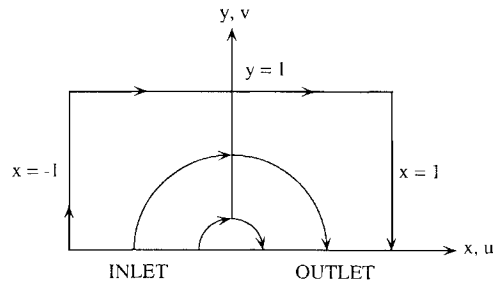

Fig. 1 Schematic of the Smith–Hutton problem.

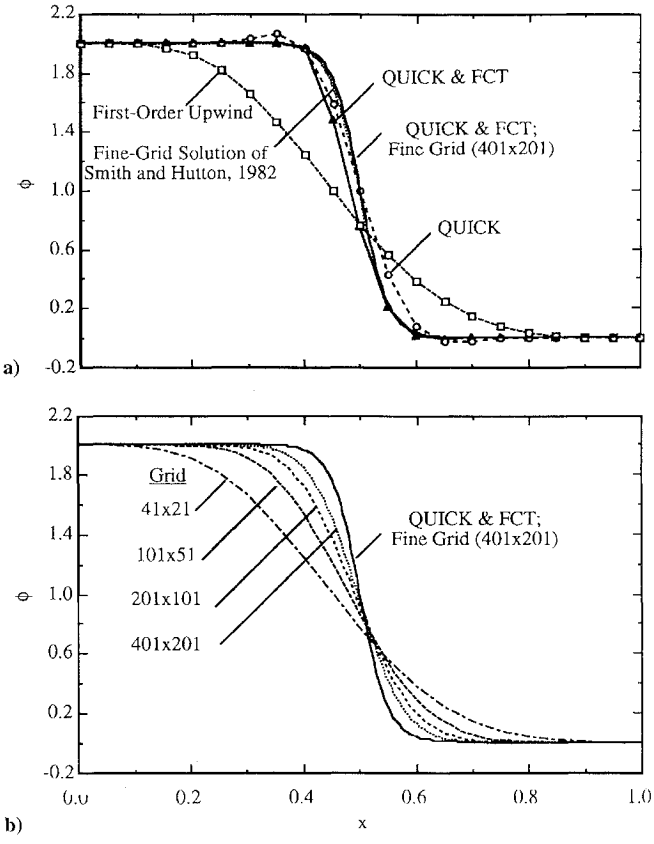

Fig. 2 Comparisons of solutions at the outlet for the Smith–Hutton problem using a) different numerical schemes and b) first-order upwind scheme and different grid distributions.

where D_i is set to 10^6 and u and v are prescribed to be

$$u = 2y(1 - x^2) \qquad v = -2x(1 - y^2) \tag{26}$$

The boundary conditions are, for $y = 0$ and $-1 \le x \le 0$ (inflow),

$$\phi = 1 + \tanh[10(2x + 1)] \tag{27}$$

and for $y = 1$ and $-1 \le x \le 1$, $x = -1$ and $0 \le y \le 1$, and $x = 1$ and $0 \le y \le 1$,

$$\phi = 1 - \tanh(10) \tag{28}$$

To be consistent with the semi-implicit feature of the current numerical model, the solution procedure adopts an explicit scheme for the convection term and an implicit scheme for the diffusion term. Three numerical schemes are tested: 1) the first-order upwind difference, 2) the QUICK scheme, and 3) the QUICK with FCT. A standard uniform grid distribution of 40 (x direction) by 20 (y direction) is used. The predicted profiles at the outflow section are compared with the fine-grid solution of Smith and Hutton[29] and the fine-grid solution of the current numerical model using the grid distribution of 401 (x direction) by 201 (y direction), Fig. 2. The fine-grid solutions of the current numerical model using the QUICK

and QUICK with FCT are nearly identical and are in excellent agreement with the fine-grid solution of Smith and Hutton (Fig. 2a). Reasonable agreement is obtained for the standard-grid solutions based on the QUICK and QUICK with FCT; however, overshoots and undershoots or spurious oscillations are seen in the solution when FCT is not applied. Figure 2a also shows significant numerical diffusion error in the solution based on the first-order upwind scheme. The numerical diffusion error progressively reduces when finer grid resolutions are used (cf. Fig. 2b); however, significant numerical diffusion error still exists even when the fine grid resolution of 401 by 201 is used. In Fig. 2a, the fine-grid solution of the current numerical model is also plotted as a reference for comparison. The Smith–Hutton test case, therefore, validates the implementation of the semi-implicit scheme in the current numerical model; the results suggest that a second-order scheme with FCT is desired for space discretization for prediction of the convection-dominated flow.

Grid Resolution

The numerical model is tested with the simulation of a ducted, axisymmetric jet diffusion flame of the classical Burke–Schumann configuration.[18] The computational domain covers a region of 500 mm in the x direction and 75 mm in the r direction. The burner (5 mm in diameter) is located at the center of the duct and is fueled by pure methane. The fuel and coflowing air are separated by an infinitely thin wall at the inlet and are maintained at 0.4 m/s for the steady and perturbed flame calculations. The Reynolds numbers based on standard-state fuel and air properties and hydraulic diameters are 1.45×10^2 and 3.700×10^3 for the fuel and air flows at the inlet, respectively. The computational domain and the standard-grid distribution of 120 (axial) $\times$ 60 (radial) are shown in Fig. 3. Note that only every other grid lines in the axial and radial directions are plotted; a quarter of the grid lines are shown. The computation uses a symmetric boundary condition for the centerline, a no-slip and impermeable wall for the outer boundary, prescribed values for the inflow condition, and a zero second-derivative for the outflow boundary. Still air is assumed to be the initial condition for the computational domain unless specified otherwise.

The uncertainty as a result of grid resolution in the calculation of the steady Burke–Schumann diffusion flame is examined. Four grid distributions are used: 120 (axial) $\times$ 60 (radial), 150 $\times$ 60, 180 $\times$ 75, and 200 $\times$ 75. The 120 $\times$ 60 is the standard grid distribution; the 150 $\times$ 60 refines the axial grid resolution near the flame tip to that equal to one-quarter of the standard resolution. The 180 $\times$ 75 refines the grids in both the axial and radial directions of the standard distribution. The 200 $\times$ 75 further refines the axial grid resolution of the 180 $\times$ 75 distribution at locations near the flame tip; a reduced grid size by 50% is obtained. A steady-state or stationary flame is predicted using

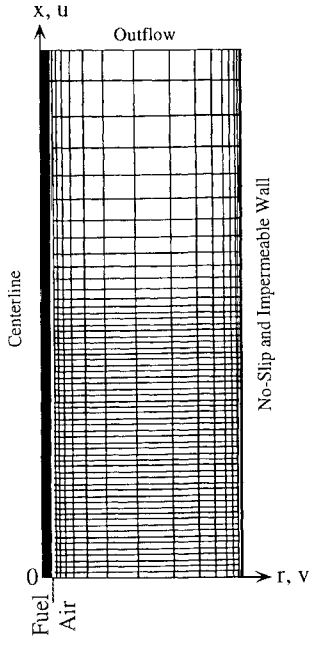

Fig. 3 Schematic of the computational domain for BSDF computation; 75 mm (radial) $\times$ 500 mm (axial) and standard grids of 120 (axial) $\times$ 60 (radial).

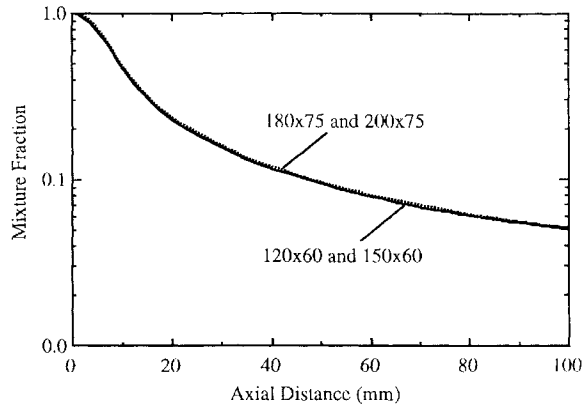

Fig. 4 Comparison of the predicted centerline mixture fractions of BSDF with fuel and air inlet velocities equal to 0.4 m/s using different grid distributions.

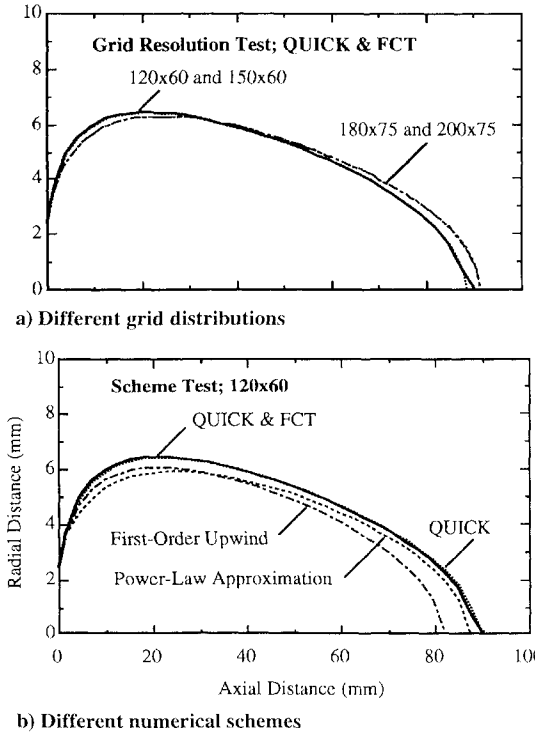

a) Different grid distributions

b) Different numerical schemes

Fig. 5 Comparison of the predicted stoichiometric surfaces of BSDF with fuel and air inlet velocities equal to 0.4 m/s.

the four grid distributions, consistent with experimental observation. The uncertainty as a result of grid resolution on the prediction of flow or flame development is illustrated by the prediction of the centerline mixture fraction shown in Fig. 4. Nearly identical mixture-fraction results are obtained for solutions using the four grid distributions. The uncertainty as a result of grid resolution on the predicted flame shape or the stoichiometric surface is illustrated in Fig. 5a. The refinements of the axial grid resolution near the flame tip do not change the prediction of the flame or flow development or the flame shape. Quantitatively, the predicted flame length is 90.3, 88.6, 91.3, and 91.5 mm for grid distributions of 120 $\times$ 60, 150 $\times$ 60, 180 $\times$ 75, and 200 $\times$ 75, respectively, in agreement with the measured luminous flame length of 91 mm. The uncertainty as a result of grid resolution in the flame length prediction using the standard-grid distribution is ± 1 grid resolution or ± 3 mm, and the use of the standard-grid distribution of 120 $\times$ 60 is judged to be adequate for the condition and the grid distributions examined.

Spatial Order of Accuracy

The importance of the spatial order of accuracy in the simulation of the Burke–Schumann diffusion flame is examined using four different numerical schemes: 1) the QUICK scheme with FCT (current

numerical model), 2) the QUICK scheme without FCT, 3) the first-order upwind, and 4) the explicit scheme with power-law approximations (i.e., the scheme adopted from Ref. 8). The grid distribution used is the standard 120×60. The marching time steps are set to 125 and 25 μs for schemes 1–3 and scheme 4, respectively. As an example, the effects on the flame shape prediction are illustrated in Fig. 5b; nearly identical flame length and shape are predicted by scheme 1, denoted by QUICK & FCT, and scheme 2, denoted by QUICK. A slightly shorter flame length and a narrower flame width are predicted by scheme 3, denoted by First-Order Upwind, and scheme 4, denoted by Power-Law Approximation. The prediction of shorter flame length and narrower flame width appears to be a result of the numerical diffusion error as a result of the lower-order accuracy in the space discretization of the upwind scheme and power-law approximations. The computational efficiency of the current numerical model, scheme 1, is improved by a factor of 3 compared with that of scheme 4, or the explicit scheme of Ref. 8. The improvement is a result of the implicit treatment of the diffusion equation, removing the restriction set by the von Neumann stability criterion. A 10-fold increase of marching time step can be used in the current numerical model.

A time-dependent laminar diffusion flame is introduced by artificial forcing of the fuel jet at the inflow boundary, i.e., at $x = 0$ mm. A low-frequency, sine wave perturbation at 1 or 2 Hz with an amplitude set to 100% of the mean velocity value is applied. The 1- or 2-Hz perturbation is chosen because the experiment conducted in our laboratory[30] shows high-frequency oscillations around 20 Hz when the fuel-jet velocity of the BSDF is perturbed at these frequencies. The numerical schemes tested for the steady flame calculation (Fig. 5b) are used to illustrate the effects of the spatial order of accuracy for simulation of the time-dependent laminar diffusion flame. The steady-state solutions of each numerical scheme are used as respective initial conditions for the time-dependent calculation.

A fundamental flame response is predicted by the four numerical schemes test; namely, the flame exhibits the same frequency as the imposed forcing frequency in such quantities as flame length, temperature, mixture fraction, and velocity. For example, the predicted flame length response during the initial or transient period of the forcing is shown in Fig. 6. A 2-Hz periodic perturbation is applied. The simulation shows a large-amplitude oscillation in response to the forcing, and the oscillation continues beyond the initial period shown by the figure. In addition to the fundamental response, the current numerical model and the QUICK scheme predict higher-frequency components (i.e., frequency higher than the imposed perturbation frequency) that superimpose on the fundamental response of the flame (cf. Fig. 6). The high-frequency components are not spurious oscillations because this is also observed in the experiment of Ref. 30.

The effects of time resolution on the simulation are illustrated in Fig. 6a. Two marching time steps of 125 μs (standard) and 25 μs (refined) are tested. A nearly identical fundamental flame response is predicted, and a slight phase shift in the high-frequency flame response is observed. The effects of grid resolution on the prediction are examined. Two grid distributions, the standard 120×60 and the refined 180×75, are used. Similar to the time resolution test, the fundamental flame response remains unchanged and a phase shift in the high-frequency flame response is predicted (Fig. 6b). The comparisons shown in Figs. 6a and 6b suggest that the standard time step and the standard grid distribution are adequate to capture the dynamic characteristics of the time-dependent Burke–Schumann diffusion flame studied. It is noted that the high-frequency response is masked by numerical diffusion error in the simulation using the first-order upwind scheme or the power-law approximations (Fig. 6c). The numerical diffusion error is quite severe; for example, only when the grid resolution is refined to 200 (axial) by 100 (radial), the higher-frequency oscillation begins to set in as shown in Fig. 7. The comparisons shown in Figs. 6 and 7 suggest that a higher-order scheme of spatial discretization is desired for simulation of the time-dependent diffusion flame examined.

To illustrate the high-frequency components in the simulation and in the experimental flame, the power spectrum density plots are shown in Fig. 8. The spectrum of the simulation is based on the time evolution of the predicted flame length. The experimental data

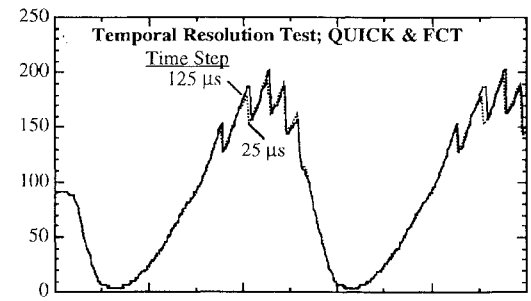

a) Different marching time steps

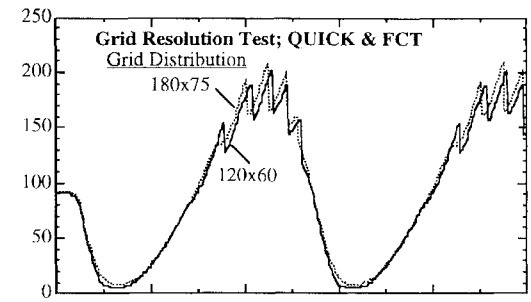

b) Different grid distributions

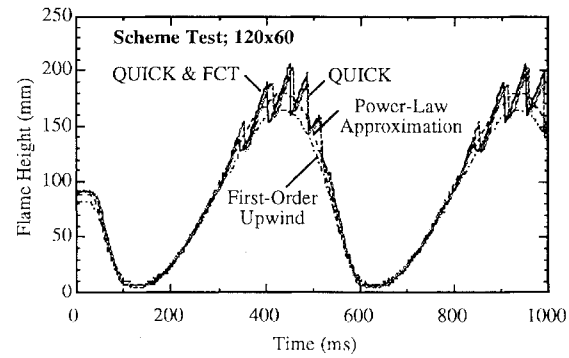

c) Different numerical schemes

Fig. 6 Comparison of the time trace of the flame height of BSDF with fuel and air inlet velocities equal to 0.4 m/s and fuel jet subject to a 2-Hz periodic perturbation.

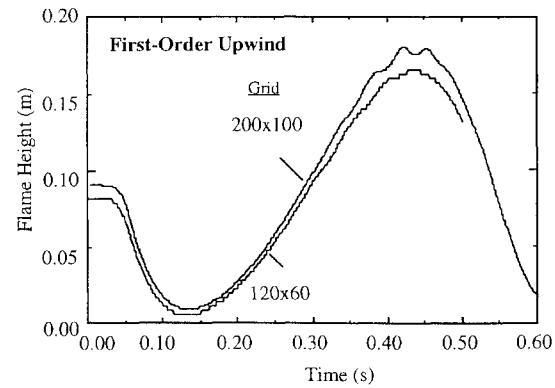

Fig. 7 Comparison of two grid distributions using an upwind scheme for prediction of the time trace of the flame height of BSDF with fuel and air inlet velocities equal to 0.4 m/s and fuel jet subject to a 2-Hz periodic perturbation.

are taken by laser deflection measurements at axial height of 125 mm above the burner.[30] The laser deflection is a result of the local refractive index change that results from the flame oscillation. The high-frequency components in the range 20–24 Hz are evident in the simulation when the QUICK scheme with or without FCT is used. The predicted high-frequency oscillation is in agreement with the experimental spectrum, in which frequency components around 22 Hz are observed.

A thorough investigation of the underlying physics responsible for the observed higher-frequency oscillation is beyond the scope of this paper. An examination of predicted vorticity contours suggests that the oscillation is a result of the interaction between the vortex formed near the flame tip (or tip vortex) and the flame and is an unsteady-flow phenomenon. As an example, Fig. 9 illustrates the predicted time evolution of the flame (stoichiometric) surface and the vorticity contour of a perturbed BSDF. The fuel and air inlet velocities are set to 0.4 m/s. A sine wave perturbation at 1 Hz with amplitude equal to 100% of the mean velocity value is imposed on the fuel-jet velocity. Five frames of the predicted flame and vorticity contours at time intervals of 0.2 s, or phase angle interval of 72 deg, are shown to illustrate the evolution during one forcing cycle. At time equal to 0 s, the fuel-jet velocity is near the lowest value. When the fuel-jet velocity increases, the flame length increases and the tip vortex is formed outside the flame, e.g., at time equal to 0.4 s shown in Fig. 9. The tip vortex convects downstream and merges with a preceding vortex in the post flame region as shown by the frames at time equal to 0.6 and 0.8 s. To illustrate the high-frequency flame oscillation and the flame tip cutting, 10 frames in the time period 0.81 to 0.90 s at time intervals of 0.01 s, or phase angle interval of 3.6 deg, are shown in Fig. 9. During this time period, the flame tip oscillates with time, although the fuel-jet velocity continues to decrease. The oscillation appears to be a result of the necking and bulging of the flame as a result of the tip vortex interaction with the flame. Periodic vortex formation near the flame tip can be seen from Fig. 9, e.g., at time equal to 0.81 and 0.86 s, and the vortex merging in the postflame region at time equal to 0.83 and 0.84 s. The simulation also shows cutting of the flame tip at time equal to 0.88 s, showing a detached flame parcel from the main body of the flame. The high-frequency flame oscillation or vortex–flame interaction, however, disappears when a forcing frequency higher than 4 Hz is applied to the fuel jet or gravity is set to zero in the computation. Therefore, the numerical simulation suggests that buoyant acceleration is essential to the observation of high-frequency flame oscillation around 20 Hz when a periodic perturbation at 1 or 2 Hz is applied to the fuel-jet velocity of an otherwise steady BSDF.

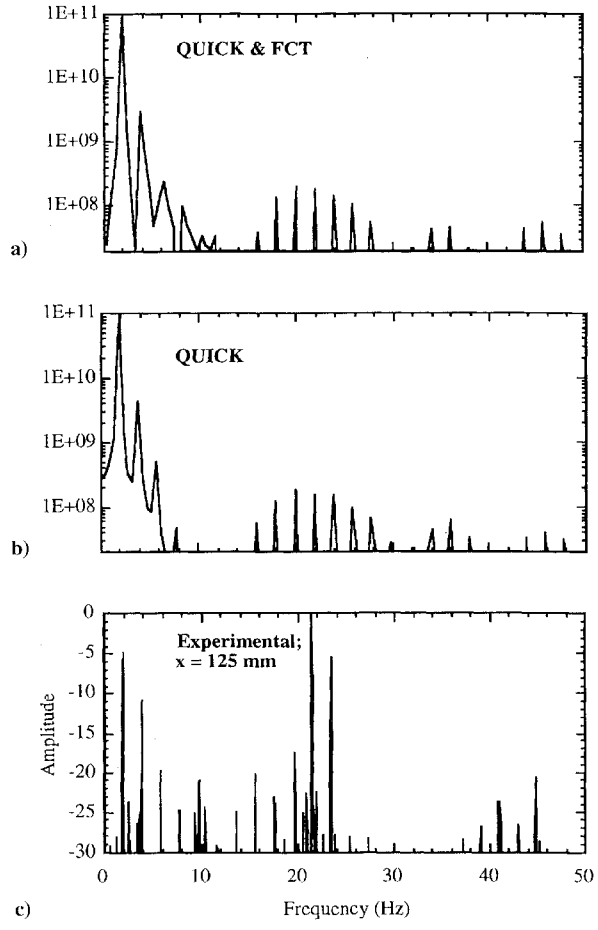

Fig. 8 Power spectrum densities of the time trace of the flame height of BSDF with fuel and air inlet velocities equal to 0.4 m/s and fuel jet subject to a 2-Hz periodic perturbation.

Summary and Conclusions

A numerical model for simulation of the time-dependent, laminar diffusion flame is presented. The numerical model uses a semi-implicit scheme for time marching and incorporates FCT for convection terms and the projection method for velocity-pressure coupling. A direct solver is used for solving the pressure Poisson equation. The numerical model is first-order accurate in time discretization and second-order in space discretization and adopts an explicit treatment for the convection term and implicit treatment for the diffusion term. The space difference scheme is based on the QUICK with FCT. Theoretical assessments are established for the order of accuracy of time discretization by viewing the projection method as an LU decomposition. Formulation is derived for the second-order accuracy of time difference. However, excessive computational times are required to achieve the second-order accuracy because the coefficient matrix of the direct solver (for pressure Poisson equation) varies at each time step. The results based on the first-order time difference scheme are shown to be adequate to resolve the dynamics of the flame considered. The semi-implicit treatment in the numerical code relaxes the time-step size restriction as a result of the von Neumann stability criterion of an explicit scheme. The time-step size is increased by 10-fold and the CPU time is decreased to one-third.

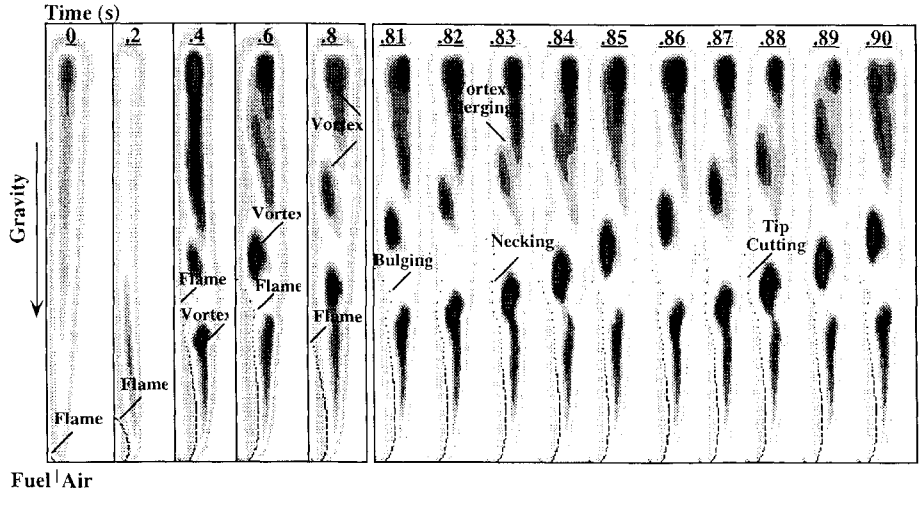

Fig. 9 Time evolution of the predicted flame (stoichiometric) surface and vorticity contours of a perturbed BSDF with fuel and air inlet velocities equal to 0.4 m/s and fuel jet subject to a 1-Hz periodic perturbation.

The numerical model is tested by computing the Smith–Hutton problem and Burke–Schumann diffusion flame with or without external forcing of the fuel jet. Four numerical schemes are examined: the second-order QUICK with FCT (current numerical model), QUICK without FCT, a first-order upwind, and a power-law approximation. The Smith–Hutton problem is used as a test case to verify the semi-implicit treatments and to assess the numerical error. The results show that significant numerical diffusion error exists in the solution based on the first-order upwind difference scheme and spurious oscillations based on the second-order QUICK scheme without FCT. For simulation of the Burke–Schumann diffusion flame with external forcing of the fuel jet, a fundamental response of the flame is predicted by all four numerical schemes tested. However, the current numerical model also predicts a high-frequency flame response around 20 Hz when a 1- or 2-Hz sine wave periodic perturbation is applied to the fuel jet. The high-frequency response is also observed in the experiment. The simulation shows that the high-frequency response is a result of periodic formations of vortex near and around the tip of the flame and the interaction with the flame. This high-frequency response disappears in the simulation when the forcing frequency is increased above 4 Hz, as well as when gravity is set to zero in the calculation. The existence of the high-frequency flame oscillation and the interaction of the flame with tip vortex is masked by numerical diffusion error resulting from the use of a first-order upwind difference scheme or power-law approximations. The present study suggests that a higher-order scheme for space difference should be used for simulation of the time-dependent laminar jet diffusion flame studied, although a first-order scheme would be adequate for time difference. The grid dependence of the flame length prediction is evaluated; the predicted flame length is within ± 1 grid or ± 3 mm for grid distributions examined.

Acknowledgments

This research was supported by the NASA Microgravity Science and Applications Division, Grant NAG3-1592, under the technical management of Dennis P. Stocker.

References

[1]Davis, R. W., Moore, E. F., Santoro, R. J., and Ness, J. R., "Isolation of Buoyancy Effect in Jet Diffusion Flame Experiments," *Combustion Science and Technology*, Vol. 73, Nos. 4–6, 1990, pp. 625–635.

[2]Davis, R. W., Moore, E. F., Roquemore, W. M., Chen, L.-D., Roquemore, W. M., and Goss, L. P., "Preliminary Results of a Numerical-Experimental Study of the Dynamic Structure of a Buoyant Jet Diffusion Flame," *Combustion and Flame*, Vol. 83, Nos. 3–4, 1991, pp. 263–270.

[3]Chen, L.-D., Vilimpoc, V., Goss, L. P., Davis, R. W., Moore, E. F., and Roquemore, W. M., "Time Evolution of a Buoyant Jet Diffusion Flame," *24th Symposium (International) on Combustion*, Combustion Inst., New York, 1992, pp. 303–310.

[4]Davis, R. W., Moore, E. F., Chen, L.-D., Roquemore, W. M., Vilimpoc, V., and Goss, L. P., "A Numerical/Experimental Study of the Dynamic Structure of a Buoyant Jet Diffusion Flame," *Theoretical and Computational Fluid Dynamics*, Vol. 6, No. 6, 1994, pp. 113–123.

[5]Leonard, B. P., "A Stable and Accurate Convective Modelling Procedure Based on Quadratic Upstream Interpolation," *Computer Methods in Applied Mechanics and Engineering*, Vol. 19, No. 1, 1979, pp. 59–98.

[6]Sharif, M. A. R., and Busnaina, A. A., "Assessment of Finite Difference Approximations for the Advection Terms in the Simulation of Practical Flow Problems," *Journal of Computational Physics*, Vol. 74, No. 1, 1988, pp. 143–176.

[7]Sharif, M. A. R., "An Evaluation of the Bounded Directional Transportive Upwind Differencing Scheme for Convection-Diffusion Problems," *Numerical Heat Transfer*, Vol. 23, Pt. B, 1993, pp. 201–219.

[8]Wu, S. H., and Chen, L.-D., "Numerical Simulation of Wick Diffusion Flames," *Journal of Propulsion and Power*, Vol. 8, No. 5, 1992, pp. 921–926.

[9]Leonard, B. P., "Simple High-Accuracy Resolution Program for Convective Modeling of Discontinuities," *International Journal for Numerical Methods in Engineering*, Vol. 30, No. 4, 1990, pp. 729–766.

[10]Katta, V. R., Goss, L. P., and Roquemore, W. M., "Effects of Nonunity Lewis Number and Finite-Rate Chemistry on the Dynamics of a Hydrogen-Air Jet Diffusion Flame," *Combustion and Flame*, Vol. 96, Nos. 1–2, 1994, pp. 60–74.

[11]Katta, V. R., Goss, L. P., and Roquemore, W. M., "Numerical Investigations on Dynamic Behavior of H2-N2 Diffusion Flame Under the Influence of Gravitational Force," AIAA Paper 92-0335, Jan. 1992.

[12]Spalding, D. B., "A Novel Finite Difference Formulation for Differential Expression Involving Both First and Second Derivatives," *International Journal for Numerical Methods in Engineering*, Vol. 4, No. 4, 1972, pp. 551–559.

[13]Boris, J. P., "A Fluid Transport Algorithm That Works," *Computing as a Language of Physics*, International Atomic Energy Agency, Vienna, 1971, pp. 171–189.

[14]Boris, J. P., and Book, D. L., "Flux Corrected Transport I. SHASTA," *Journal of Computational Physics*, Vol. 11, No. 1, 1973, pp. 38–69.

[15]Ellzey, J. L., Laskey, K. J., and Oran, E. S., "A Study of Confined Diffusion Flames," *Combustion and Flame*, Vol. 84, Nos. 3–4, 1991, pp. 249–264.

[16]Patnaik, G., Guirguis, R. H., Boris, J. P., and Oran, E. S., "A Barely Correction for Flux-Corrected Transport," *Journal of Computational Physics*, Vol. 71, No. 1, 1987, pp. 1–20.

[17]Kaplan, C. R., Baek, S. W., Oran, E. S., and Ellzey, J. L., "Dynamics of a Strong Radiating Unsteady Ethylene Jet Diffusion Flame," *Combustion and Flame*, Vol. 96, Nos. 1–2, 1994, pp. 1–21.

[18]Burke, S. P., and Schumann, T. E. W., "Diffusion Flames," *Industry and Engineering Chemistry*, Vol. 20, No. 10, 1928, pp. 998–1004.

[19]Williams, F. A., *Combustion Theory: The Fundamental Theory of Chemically Reacting Flow Systems*, Benjamin/Cummings, Menlo Park, CA, 1985.

[20]Hyer, P. V., Stocker, D. P., and Clark, I. O., "Comparison of Numerical Model Results with Diffusion Flames in Microgravity," AIAA Paper 93-0707, Jan. 1993.

[21]Patankar, S. V., *Numerical Heat Transfer and Fluid Flow*, Hemisphere, Washington, DC, 1980.

[22]Peyrot, R., and Taylor, T. D., *Computational Methods for Fluid Flow*, Springer–Verlag, New York, 1983.

[23]Perot, J. B., "An Analysis of the Fractional Step Method," *Journal of Computational Physics*, Vol. 108, No. 1, 1993, pp. 51–58.

[24]Kim, J., and Moin, P., "Application of a Fractional-Step Method to Incompressible Navier–Stokes Equations," *Journal of Computational Physics*, Vol. 59, No. 2, 1985, pp. 308–323.

[25]Laverdant, A. M., and Candel, S. M., "A Numerical Analysis of a Diffusion Flame-Vortex Interaction," *Combustion Science and Techonology*, Vol. 60, Nos. 1–3, 1988, pp. 79–96.

[26]Zalesak, S. T., "Fully Multidimensional Flux-Corrected Transport Algorithm for Fluids," *Journal of Computational Physics*, Vol. 31, No. 3, 1979, pp. 335–362.

[27]Anderson, D. A., Tannehill, J. C., and Pletcher, R. H., *Computational Fluid Mechanics and Heat Transfer*, Hemisphere, Washington, DC, 1984.

[28]Kunhardt, E. E., and Wu, C., "Toward a More Accurate Flux Corrected Transport Algorithm," *Journal of Computational Physics*, Vol. 68, No. 1, 1987, pp. 127–150.

[29]Smith, R. M., and Hutton, A. G., "The Numerical Treatment of Advection: A Performance Comparison of Current Methods," *Numerical Heat Transfer*, Vol. 5, No. 4, 1982, pp. 439–461.

[30]Bang, H.-N., "An Experimental Investigation of Jet Diffusion Flames: Flame Response and Stabilization in Cross-Flow," M.S. Thesis, Dept. of Mechanical Engineering, Univ. of Iowa, Iowa City, IA, 1996.